

# Unconventional Rotor Power Response to Yaw Error Variations

S. J. Schreck<sup>1</sup> and J. G. Schepers<sup>2</sup>

<sup>1</sup>NREL's National Wind Technology Center, United States

<sup>2</sup>Energy Research Center of the Netherlands, The Netherlands

Email: scott.schreck@nrel.gov

**Abstract.** Continued inquiry into rotor and blade aerodynamics remains crucial for achieving accurate, reliable prediction of wind turbine power performance under yawed conditions. To exploit key advantages conferred by controlled inflow conditions, EU-JOULE DATA Project and UAE Phase VI experimental data were used to characterize rotor power production under yawed conditions. Anomalies in rotor power variation with yaw error were observed, and the underlying fluid dynamic interactions were isolated. Unlike currently recognized influences caused by angled inflow and skewed wake, which may be considered potential flow interactions, these anomalies were linked to pronounced viscous and unsteady effects.

## 1. Introduction

Wind turbine power performance remains a crucial research topic and has grown considerably with time. Beginning with foundations in blade and rotor aerodynamics, inquiry has broadened and now encompasses larger scale phenomena like wind plant wakes and the atmospheric boundary layer. Current estimates of wind plant underperformance range from 1% to 10%, and potential benefits of pertinent research are substantial. To address these shortfalls, aerodynamic phenomena across the entire spatio-temporal spectrum, from the blade and rotor to the wind plant and atmospheric boundary layer, need to be considered as potential targets for performance improvement.

Earlier work on the National Renewable Energy Laboratory's (NREL's) Combined Experiment Rotor (CER), a predecessor to the Unsteady Aerodynamics Experiment (UAE) Phase VI, showed that adding simulated insect roughness to the rotor reduced power performance by 7% to 9%, for blades using the roughness tolerant S809 airfoil.[1] Related work showed more serious losses for conventional airfoils, like the NACA four and five digit series cross sections.[2] Though these efforts were carried out at subscale, work by Braslow et al. [3] suggests that results should remain relevant at higher Reynolds numbers.

Subsequently, a phenomenon termed 'double stall' was isolated, which produced two or more distinct power levels at high wind speeds in response to otherwise identical wind inflow and turbine operating conditions.[4] Double stall was thoroughly investigated and the underlying



physics identified using full-scale rotor measurements, wind tunnel experiments, and detailed computations.

Along with these and other blade aerodynamic phenomena, the effects of rotor yaw error also must be considered significant. Inflow shear, turbulence, and wake effects preclude the existence of stable axisymmetric operation, and so field operation generally amounts to continuously yawed operation. In this direction, Schepers [5] observed that yaw aerodynamics can be more productively studied by means of wind tunnel measurements, which are done under known stationary and uniform conditions, which can be more helpful in understanding yaw aerodynamics.

To complement test and experiments in this area, earlier work by Dahlberg and Montgomerie [6] hypothesized that rotor power production varied according to a cosine function, and used field and wind tunnel measurements to calibrate this relationship. Similarly, subsequent research by Schepers [7] using wind tunnel data found that rotor power varied consistent with a cosine function. Notably, both of these efforts found that turbine rotor power varied monotonically with yaw error.

However, recent analyses of wind tunnel data acquired in connection with the NREL UAE Phase VI and the EU-JOULE DATA Project showed rotor power response with yaw error that varied in strong nonmonotonic fashion with yaw error. Notably, these results revealed that rotor power at nonzero yaw error can exceed that at zero yaw by large margins. This effort will characterize this unconventional, nonmonotonic behavior in detail, and will identify the underlying aerodynamics that cause it.

## 2. Experimental Methods

### 2.1 EU-JOULE DATA Project Turbine

EU-JOULE DATA Project testing was carried out in the DNW LLF 9.5 m x 9.5 m open jet, and has been documented by Schepers.[7] The DATA Project focused on aeroacoustic effects, but the power also was measured at axisymmetric and yawed conditions. In these experiments, a reference rotor and two acoustically optimized rotors were employed. All three rotors had two blades and diameters of 4.5 m.

Blade airfoils were as follows for the reference rotor: in the radial range  $0.0 \text{ m} \leq r \leq 0.5 \text{ m}$ , no aerodynamic profiles were prescribed or modeled; in the range  $0.5 \text{ m} \leq r < 0.9 \text{ m}$ , the DU91-W2-250 airfoil was used; in the range  $0.9 \text{ m} \leq r < 1.2 \text{ m}$ , the FFA-W3-211 airfoil was used; and in the range  $1.2 \text{ m} \leq r \leq 2.25$

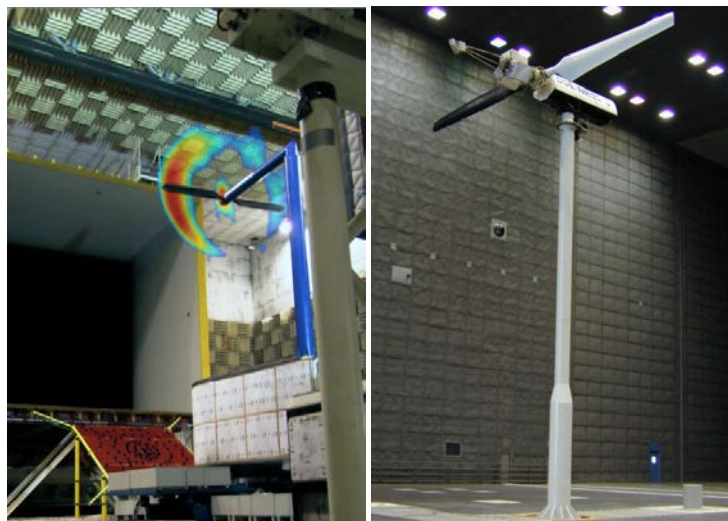


**Figure 1.** EU-JOULE Project DATA turbine mounted in DNW 9.5 m x 9.5 m wind tunnel (left) and UAE Phase VI turbine mounted in NASA Ames 24.4 m x 36.6 m wind tunnel (right).

m, the NACA64-418 airfoil was used. The two acoustically optimized rotors used special purpose low noise airfoils.

The DATA Project blade had a constant chord of 0.24 m and a twist of  $10^\circ$  from root to tip. Reynolds number at the blade tip was  $1.7 \times 10^6$ . Blade geometry and operating conditions were dictated by the need to assess the performance of the low noise airfoils, which were located at the outer radial part of the blade for the two acoustically optimized rotors.

A cylindrical tower that was 0.406 m in diameter held the nacelle 5.3 m above the platform base, with a 3.0 m overhang. This overhang situated the rotor axis at the jet centerline and placed the rotor well upwind of the tower. The DATA Project turbine is shown in the left panel of Figure 1, in the DNW LLF 9.5 m x 9.5 m open jet. Power was derived using torque measurements from a torque meter mounted in the hub, along with rpm data.

### 2.1 UAE Phase VI Turbine

Several UAE Phase VI configurations were tested in the NASA Ames 24.4 m x 36.6 m wind tunnel, and are described by Hand et al.[8] Data analyzed herein were acquired from a two-bladed upwind rotor, 10.1 m in diameter, with zero cone angle. The rotor turned clockwise (viewed from downwind) at a constant 71.6 rpm, was stall regulated, and had a maximum rated power of 19.8 kW. A cylindrical tower that was 0.4 m in diameter supported the turbine at a hub height of 12.2 m (test section centerline), with a 1.32 m rotor overhang. This UAE Phase VI configuration, mounted in the NASA Ames 24.4 m x 36.6 m wind tunnel, is shown in the right panel of Figure 1.

The black blade on the left side of the UAE Phase VI rotor in Figure 1 was equipped with five full pressure tap rows to acquire detailed surface pressure data. A full pressure tap distribution consisted of 22 taps distributed over the pressure and suction surfaces of the blade.

Pressure taps were more densely distributed near the blade leading edge to better resolve the pronounced gradients typically present there. Figure 2 shows the UAE Phase VI full pressure tap distributions that were located at  $r/R = 0.30, 0.47, 0.63, 0.80$ , and  $0.95$ .

Dynamic pressures and inflow angles were measured near these five pressure tap distributions using five hole probes. These probes were mounted on cylindrical stalks at  $0.34R, 0.51R, 0.67R, 0.84R$ , and  $0.91R$ , with the probe tip  $0.8c$  upstream of the blade leading edge. Probes were angled  $20^\circ$  downward relative to the local chord line, allowing measurement of local flow angles between  $-15^\circ$  and  $55^\circ$ . Local inflow angles measured by the five hole probes were converted to section angles of attack ( $\alpha$ ) using an experimentally derived upwash correction.[9]

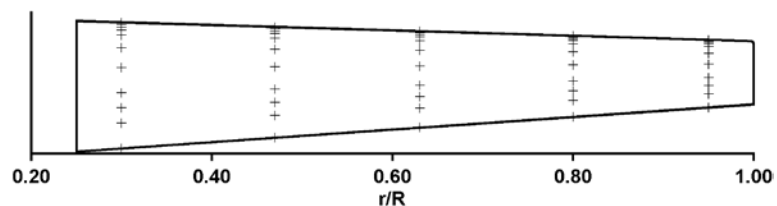


**Figure 2. UAE Phase VI blade planform drawing with suction surface tap locations. Leading edge is at the top of the planform.**

The blades used throughout the NASA Ames wind tunnel test were both twisted and tapered. The blade taper distribution is shown in Figure 2, with the maximum blade chord being 0.737 m at 0.25R, and tapering to 0.356 m at the tip. Figure 3 shows the blade twist, which decreases from 21.8° at 0.25R to 0.0° at the tip. Between 0.25R and the tip, blade cross section was uniform, corresponding to the S809 airfoil. Design procedures, constraints, and measures of merit for this blade have been documented in detail.[10]

Time records of  $c_p$  were integrated over the sectional chord to obtain time records of  $C_n$  and  $C_t$ . The sectional torque coefficient  $C_{TQ}$  was defined as the projection of  $C_n$  and  $C_t$  into the rotor plane. Rotor power was derived using low speed shaft torque from strain gage measurements and rotor speed data. Test section flow speed and air properties were measured using the 24.4 m x 36.6 m wind tunnel air data system.[11]

### 3. Results and Discussion

#### 3.1 Cycle mean $C_p$

Anomalous rotor power responses to yaw error variations have been observed in experimental data alone and in connection with model predictions. Figure 4 shows EU-JOULE DATA Project rotor results ( $U_\infty = 14$  m/s,  $U_{TIP} = 100$  m/s) and blade element momentum theory predictions previously reported in connection with the EU-JOULE DATA Project.[7] In Figure 4, each data point corresponds to an average derived from 35 successive rotor revolutions. In comparing the measured and predicted data, two trends are apparent. First, at  $\gamma = 0^\circ$ , blade element momentum theory overpredicts the rotor power by approximately 8%. Second, as  $\gamma$  decreases toward  $-25^\circ$ , measured data decrease with  $\gamma$  according to  $\cos^{1.8}(\gamma)$ , whereas the predicted drop in power is delayed to lower  $\gamma$ . Of particular note is the slight increase in measured  $C_p$  as  $\gamma$  goes from  $0^\circ$  to  $-5^\circ$ , which precedes the sustained decrease in measured  $C_p$  as  $\gamma$  decreases from  $-5^\circ$  to  $-25^\circ$ . Though subtle, this nonmonotonic response was confirmed by more pronounced trends in UAE Phase VI data, in contrast to previous results.[6]

Figure 5 shows UAE Phase VI rotor  $C_p$  versus  $\gamma$ , for three  $U_\infty$  values and blade pitch =  $3.0^\circ$  (H Sequence). In Figure 5, each data point is an average derived from approximately 38

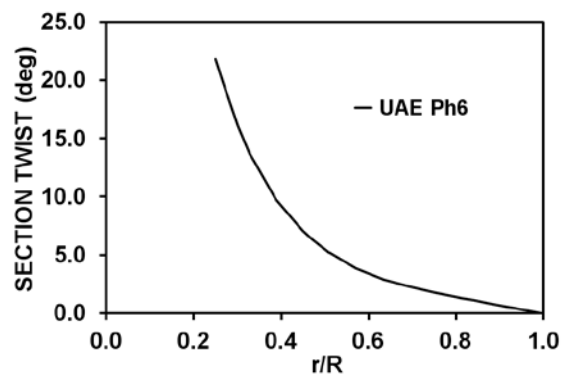


Figure 3. Sectional blade twist for the aerodynamically active part of the UAE Phase VI blade.

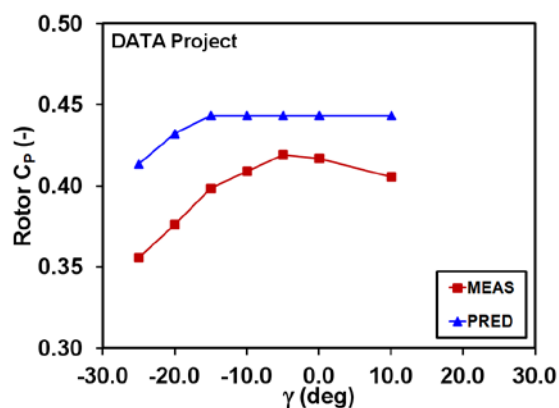


Figure 4. Measured and predicted  $C_p$  vs.  $\gamma$  for DATA Project for  $U_\infty = 14$  m/s.

successive rotor revolutions. Consistent with conventional behavior, at  $U_\infty = 7$  m/s rotor  $C_p$  is maximum at  $\gamma = 0^\circ$ , at a value of 0.36, and decreases monotonically for higher and lower  $\gamma$ . Anomalous behavior occurs at  $U_\infty = 10$  m/s, where rotor  $C_p$  exhibits a local minimum of 0.20 at  $\gamma = 0^\circ$ , rises to absolute maxima of approximately 0.22 at  $\gamma = 10^\circ$  and  $\gamma = -10^\circ$ , and then decreases with greater  $\gamma$  magnitude. The trend at  $U_\infty = 15$  m/s is again anomalous and similar to that at 10 m/s, with rotor  $C_p$  at a local minimum of 0.06 at  $\gamma = 0^\circ$ , increasing to absolute maxima of 0.08 at  $\gamma = 30^\circ$  and  $\gamma = -30^\circ$ , and then decreasing with greater  $\gamma$  magnitude.

Clearly, the  $U_\infty = 7$  m/s data decrease monotonically with  $\gamma$ , consistent with a cosine function. However, data for  $U_\infty = 10$  m/s and 15 m/s show strong nonmonotonic responses, confirming prior DATA Project trends (cf. above).

### 3.2 Segmented rotor $C_p$

To isolate the sources of the  $C_p$  anomalies observed in Figure 5, the blade was subdivided into five radial segments, with the radial segments demarcated such that the five pressure tap rows were centered in each of the five radial segments. Then, segmented rotor  $C_p$  was calculated for each of the five segments, across the same range of  $U_\infty$  and  $\gamma$  as shown in Figure 5. This was done using  $C_{TQ}$  and rotor rpm data. This procedure excluded contributions of viscous drag to  $C_p$ , which did not alter conclusions in this study. Results are shown in Figures 6–8.

Figure 6 shows segmented rotor  $C_p$  for  $U_\infty = 7$  m/s. At this  $U_\infty$ , aggregate rotor  $C_p$  response in Figure 5 was conventional and exhibited no anomalous nonmonotonicity with  $\gamma$ . Figure 6 shows that segmented rotor  $C_p$  for all five radial locations was similarly conventional, with rotor  $C_p$  being maximal at  $\gamma = 0^\circ$  and decreasing monotonically with  $\gamma$  for all five radial locations. Generally, radial locations farther outboard yielded higher  $C_p$  levels, with  $C_p$  at 0.95R lying below that for 0.80R caused by tip loss.

Figure 7 shows segmented rotor  $C_p$  for  $U_\infty = 10$  m/s. At  $U_\infty = 10$  m/s, the Figure 5 aggregate rotor  $C_p$  response was visibly nonmonotonic with  $\gamma$ , attaining a global maximum for  $\gamma = 10^\circ$ , with lower values of  $C_p$  at lower and higher values of  $\gamma$ . Figure 7 shows that the segmented rotor  $C_p$  displayed similar nonmonotonic character at 0.47R and 0.63R. These two radial locations exhibited a maximum segmented rotor  $C_p$  at  $\gamma = 10^\circ$ , as did aggregate rotor response in

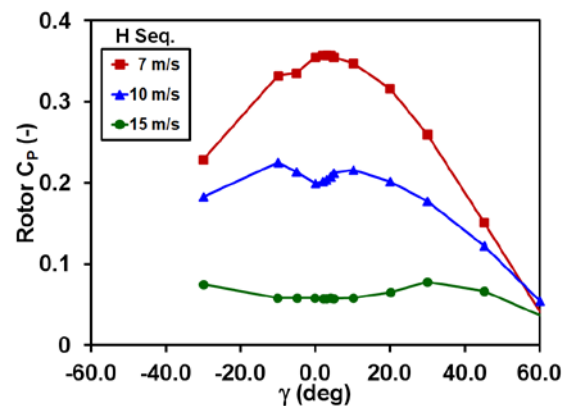


Figure 5.  $C_p$  vs.  $\gamma$  for UAE Phase VI for  $U_\infty = 7, 10$ , and 15 m/s.

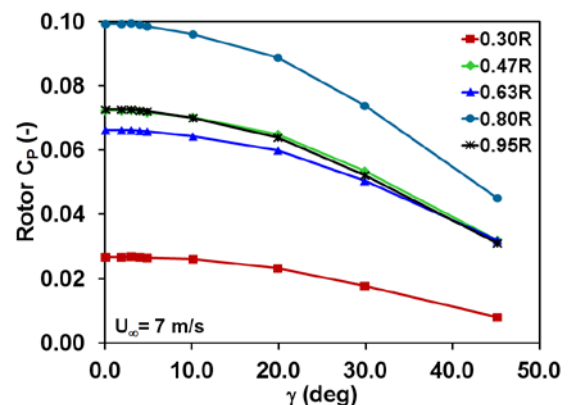


Figure 6. Segmented rotor  $C_p$  vs.  $\gamma$  for  $U_\infty = 7$  m/s.



Figure 5. In contrast, segmented rotor  $C_p$  was conventionally monotonic at 0.30R, 0.80R, and 0.95R. Together, these data indicated that the rotor aerodynamic interactions responsible for unconventional  $C_p$  yaw response at  $U_\infty = 10$  m/s occurred around 0.47R and 0.63R, near the blade central region.

Figure 8 shows segmented rotor  $C_p$  for  $U_\infty = 15$  m/s. At this test section speed, the Figure 5 aggregate rotor  $C_p$  response was strongly nonmonotonic with  $\gamma$ , exhibiting a global maximum at  $\gamma = 30^\circ$  and decreasing for both lower and higher  $\gamma$  values. Figure 8 shows that segmented rotor  $C_p$  also was strongly nonmonotonic at 0.30R, 0.47R, 0.63R, and 0.80R, with only 0.95R responding with  $\gamma$  in conventional fashion.

In Figure 8 at the four inboard locations, segmented rotor  $C_p$  response with  $\gamma$  varied significantly. At 0.30R, segmented rotor  $C_p$  reached a maximum at  $\gamma = 10^\circ$  and decreased gradually for higher and lower  $\gamma$  values. At 0.47R,  $C_p$  increased linearly and gradually through the range  $0^\circ \leq \gamma \leq 20^\circ$ , rose more steeply from  $\gamma = 20^\circ$  to  $\gamma = 30^\circ$ , and thereafter again increased more gradually. At 0.63R,  $C_p$  first declined linearly through  $0^\circ \leq \gamma \leq 10^\circ$ , and then increased linearly though more gradually for higher  $\gamma$  values. At 0.80R, segmented rotor  $C_p$  increased substantially though nonuniformly through the range  $0^\circ \leq \gamma \leq 30^\circ$ , and decreased marginally for  $\gamma = 45^\circ$ . Notably, none of the Figure 8 segmented rotor  $C_p$  plots for 0.30R, 0.47R, 0.63R, or 0.80R resembled the aggregate rotor  $C_p$  plot for  $U_\infty = 15$  m/s shown in Figure 5. This testifies to the complex interactions and competing influences that dictated aggregate rotor  $C_p$ . These data indicated that the rotor fluid dynamics responsible for nonmonotonic  $C_p$  yaw response at  $U_\infty = 15$  m/s took place across the range  $0.30 \leq r/R \leq 0.80$ .

### 3.3 Zero yaw rotor baseline

As discussed above, both aggregate and segmented rotor  $C_p$  variations with  $\gamma$  were assessed relative to  $C_p$  levels at  $\gamma = 0^\circ$ . Thus, blade flow field state at  $\gamma = 0^\circ$  was examined to establish a baseline for flow field modifications in response to  $\gamma$ .

Figure 9 shows  $\alpha$  across the blade radius, for  $U_\infty = 7, 10$ , and 15 m/s. To obtain  $\alpha$  data, an experimentally derived upwash correction [9] was applied to local inflow angle data, which were measured by the five hole probes and ensemble averaged over the 30 s data set duration. The dashed horizontal line that crosses the figure at  $\alpha = 15.2^\circ$  represents the S809 stall threshold

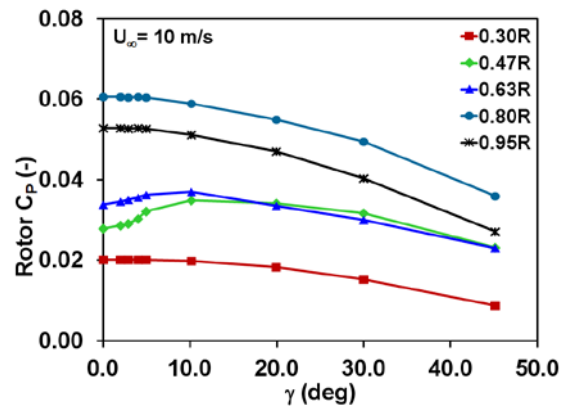


Figure 7. Segmented rotor  $C_p$  vs.  $\gamma$  for  $U_\infty = 10$  m/s.

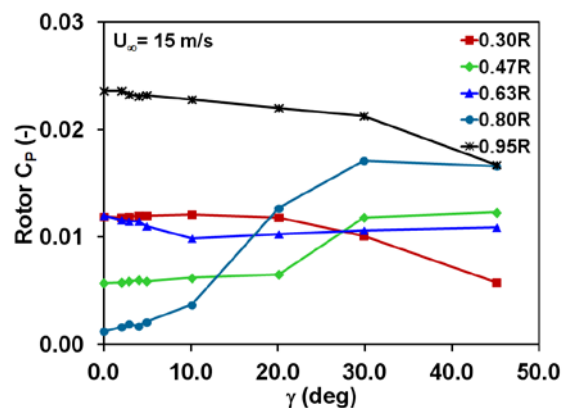


Figure 8. Segmented rotor  $C_p$  vs.  $\gamma$  for  $U_\infty = 15$  m/s.

for two-dimensional, static conditions.[12] Figure 9 shows that all five radial locations operated below stall conditions at  $U_\infty = 7$  m/s, and all locations operated above stall at  $U_\infty = 15$  m/s. At  $U_\infty = 10$  m/s, the 0.30R and 0.47R locations experienced  $\alpha$  levels above stall, and the remaining radial locations outboard were subjected to  $\alpha$  levels below stall.

To gauge blade aerodynamic response to Figure 9  $\alpha$  levels,  $C_n$  was adopted as a general indicator of blade aerodynamic activity.  $C_n$  data acquired at the five tap rows were averaged over the 30 s data set, and the mean data plotted in Figure 10. In Figure 10, the dashed horizontal line at  $C_n = 1.01$  represents the S809 stall threshold under static, two-dimensional conditions.[12] Here, it is apparent that  $C_n$  levels for  $U_\infty = 7$  m/s were below the stall  $C_n$  threshold, which was consistent with  $\alpha$  levels for  $U_\infty = 7$  m/s in Figure 9 that were below stall. Likewise, the  $C_n$  values at 0.63R, 0.80R, and 0.95R for  $U_\infty = 10$  m/s were below the stall  $C_n$  threshold, which was consistent with  $\alpha$  levels below stall at these radii for  $U_\infty = 10$  m/s in Figure 9. For  $U_\infty = 15$  m/s at 0.80R and 0.95R in Figure 10,  $C_n$  values lie slightly below stall level, consistent with  $\alpha$  levels in Figure 9 that were slightly above stall. This represents a post-stall response consistent with two-dimensional, static conditions.

In Figure 10, it is notable that  $C_n$  for  $U_\infty = 10$  m/s at 0.30R and 0.47R, and for  $U_\infty = 15$  m/s at 0.30R, 0.47R, and 0.63R exceeded stall  $C_n$  levels in response to Figure 9  $\alpha$  levels that were substantially greater than the stall  $\alpha$  threshold. Ordinarily,  $\alpha$  levels above the stall threshold would produce post-stall  $C_n$  levels below stall  $C_n$ . This apparent inconsistency reflects a clear departure from conventional, two-dimensional aerodynamics, which was supplanted by three-dimensional rotational augmentation.[13] This is an important observation, as it shows the disparity between  $C_p$  levels at axisymmetric and yawed conditions is not simply caused by depressed aerodynamic activity at  $\gamma = 0^\circ$ . On the contrary, Figures 9 and 10 show that  $\gamma = 0^\circ$  aerodynamic activity is amplified above two-dimensional levels by rotational augmentation. This confirms the strength of the additional augmentation that occurred for  $\gamma > 0^\circ$

### 3.4 Sectional blade aerodynamics

Figures 9 and 10 indicated that rotational augmentation, an event strongly governed by viscous effects, was present at  $\gamma = 0^\circ$ . Examination of the surface pressure data for  $\gamma > 0^\circ$  revealed the presence of two other viscous dominated phenomena described below. One of them, dynamic stall, has been observed over much of the UAE Phase VI turbine operating envelopes.[14]

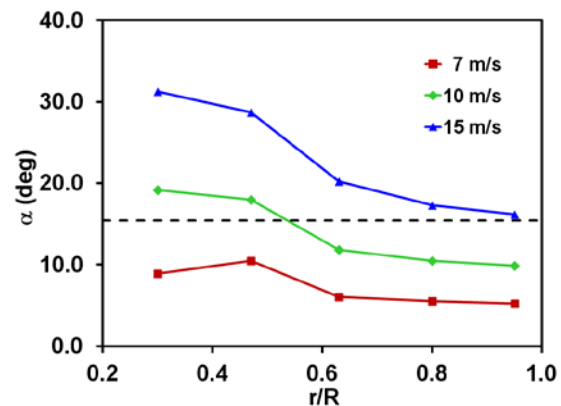


Figure 9.  $\alpha$  vs.  $r/R$  for  $U_\infty = 7, 10, 15$  m/s.

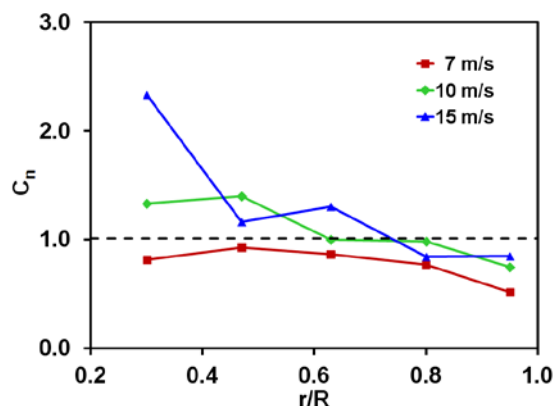
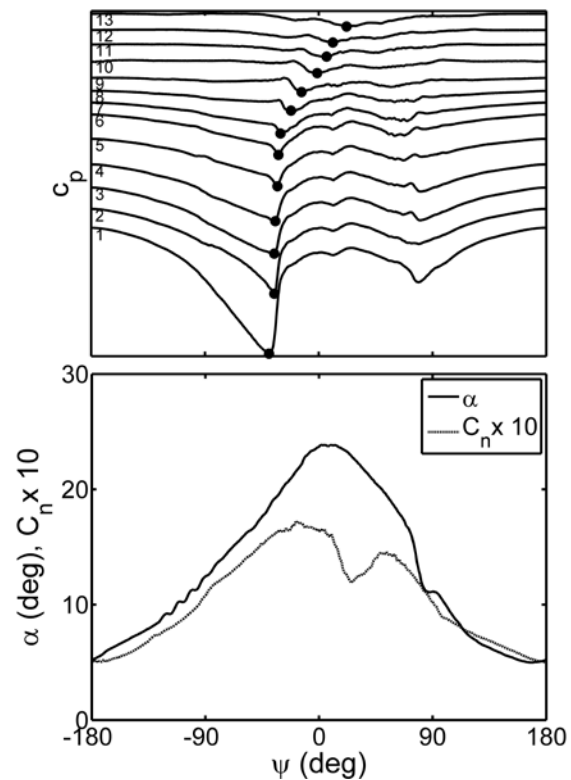


Figure 10.  $C_n$  vs.  $r/R$  for  $U_\infty = 7, 10, 15$  m/s.

Dynamic stall data typical of those used in the current effort are shown in Figure 11, for  $U_\infty = 10$  m/s and  $\gamma = 45^\circ$ , at blade radial location 0.47R. In the upper panel, traces 1 through 13 are plotted with rotor azimuth ( $\Psi$ ), representing  $c_p$  at 13 pressure taps from the blade leading edge to trailing edge on the blade suction surface. The 13 traces have been offset vertically to enable viewing, and zero references have been omitted. Surface pressure minima corresponding to dynamic stall vortex passage [15–17] have been marked with filled circles. The lower panel in Figure 11 shows sectional angle of attack ( $\alpha$ ) and  $C_n \times 10$  over the same  $\Psi$  range. Increasing blade azimuth represents counterclockwise blade rotation as viewed from upwind, with  $\Psi = 0^\circ$  azimuth representing the instrumented blade at the 12 o'clock position. The  $c_p$  and  $\alpha$  data shown in Figure 11 are ensemble averages derived from approximately 38 consecutive rotor cycles.

In Figure 11, angle of attack started at  $\alpha = 5.3^\circ$  at  $\Psi = -180^\circ$ , and 0.437 seconds later peaked at  $\alpha = 23.9^\circ$  at  $\Psi = 6.9^\circ$ . Simultaneously,  $C_n$  increased steeply, peaked at  $C_n = 1.71$  at  $\Psi = -18.9^\circ$ , briefly decreased and underwent a resurgence, and finally decreased to  $C_n = 1.0$  at  $\Psi = 180^\circ$ . This  $C_n$  peak level significantly exceeded the S809 stall  $C_n$  of 1.05, consistent with dynamic stall. As  $\alpha$  increased,  $c_p$  decreased at all 13 pressure taps, declining most rapidly with  $\alpha$  at the leading edge tap. The leading edge tap reached a minimum of  $c_p = -9.84$  at  $\Psi = -38.9^\circ$ , signaling initiation of the leading edge vortex. Subsequently,  $c_p$  variations during  $-35.6^\circ \leq \Psi \leq -33.1^\circ$  produced deep, narrow  $c_p$  troughs at taps 1 through 6, implying passage of a relatively condensed vortex structure. Thereafter, taps 7 through 13, showed broad, shallow depressions with time, indicating passage of a more expansive vortex structure. Broadening of the vortex passage signatures was accompanied by reductions in  $c_p$  magnitudes, with the minimum  $c_p$  at tap 13, occurring at  $\Psi = 21.7^\circ$ , being -0.79. The  $c_p$  minima consistently occurred at later times for taps farther aft on the blade chord. This response is consistent with a dynamic stall vortex that initiated near the leading edge, and then convected aft toward the trailing edge.



**Figure 11. Suction surface  $c_p$  and  $\alpha$  histories for  $U_\infty = 10$  m/s and 0.47R, at  $\gamma = 45^\circ$ .**



Figure 12 documents a second dynamic event found to be important in the current investigation. Data in Figure 12 correspond to  $U_\infty = 15$  m/s and  $\gamma = 20^\circ$ , at blade radial location 0.30R. The upper and lower panels in Figure 12 are formatted in the same way as in Figure 11, and the data were derived using the same procedures.

In Figure 12, angle of attack started at  $\alpha = 19.2^\circ$  at  $\Psi = -180^\circ$ , and 0.462 s later peaked at  $\alpha = 58.6^\circ$  at  $\Psi = 19.7^\circ$ . Simultaneously,  $C_n$  increased steeply, reached  $C_n = 2.46$  at  $\Psi = -65.8^\circ$ , and remained relatively level until  $\Psi = 77.1^\circ$ , when  $C_n$  began to decrease again. It is noteworthy that during  $-65.8^\circ \leq \Psi \leq 77.1^\circ$  when  $C_n$  was nearly constant,  $\alpha$  rose and fell substantially through the range  $33.6^\circ \leq \alpha \leq 58.6^\circ$ .  $C_n$  appeared closely correlated with forward movement of the  $c_p$  minimum marked by the filled circles in the upper panel of Figure 12. During  $-20.7^\circ \leq \Psi \leq 152.7^\circ$ , this feature moved forward from the trailing edge to the leading edge. In contrast to the leading edge vortex signature in Figure 11, the feature in Figure 12 remained broad and shallow, and  $c_p$  levels varied less, remaining between -2.0 and -6.0. Distinct from a dynamic stall event, these kinematics are more consistent with a rotationally augmented state interrupted by the forward movement of dynamic separation.

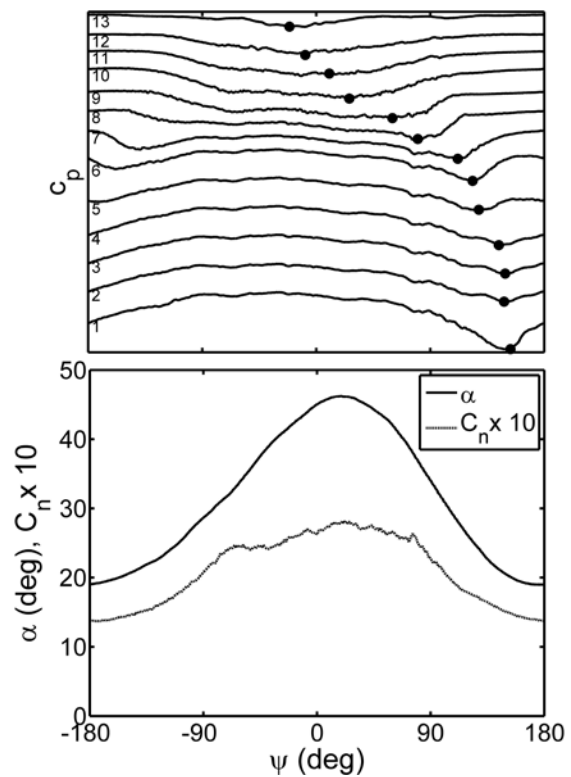


**Figure 12. Suction surface  $c_p$  and  $\alpha$  histories for  $U_\infty = 15$  m/s and 0.30R, at  $\gamma = 20^\circ$ .**

### 3.5 Sectional blade torque coefficient

To understand the trends above in segmented  $C_p$ , the underlying rotor aerodynamics were examined using sectional torque coefficient ( $C_{TQ}$ ) as an index of sectional blade aerodynamic activity. The sectional torque coefficient  $C_{TQ}$ , was defined as the projection of  $C_n$  and  $C_t$  into the rotor plane. This quantity was chosen because it simultaneously provided an index for the magnitude of rotor torque and furnished an indicator for the presence and intensity of blade flow field activity. Described below are two stereotypical  $C_{TQ}$  events found to be generally responsible for key the segmented  $C_p$  maxima shown in Figures 6 through 8.

Figure 13 includes four plots of  $C_{TQ}$  with  $\Psi$ , for  $U_\infty = 10$  m/s and  $\gamma = 5^\circ, 10^\circ, 20^\circ$ , and  $30^\circ$ , all at blade radial station 0.47R. In the upper left part of the plot, four large crosses are superimposed and circumscribed by a dashed rectangle marked “LEV Initiation”. These four crosses identify the times when leading edge vortex initiation occurred for the four  $\gamma$ , consistent with the criteria explained in connection with Figure 11. Near the center of the plot, four other large crosses appear and are surrounded by a dashed rectangle marked “LEV at 0.56c”. These four crosses identify the times when the leading edge vortex was observed passing pressure tap 10 located at 0.56c at the four  $\gamma$ , again as explained in connection with Figure 11.

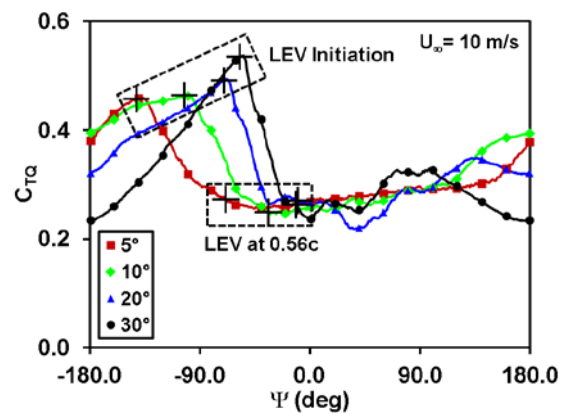
In Figure 13, increasing  $\Psi$  in connection with  $\gamma > 0$  dynamically increased angle of attack ( $\alpha$ ) in the first half of the rotor cycle. In Figure 11, this produced leading edge vortex initiation near the blade leading edge, downstream convection over the suction surface, and ultimate shedding from the trailing edge, which caused  $C_n$  to rise, peak, and finally drop.

A similar progression is shown in Figure 13, with  $C_{TQ}$  being the analog of  $C_n$ . At  $\Psi = 0^\circ$ ,  $C_{TQ}$  begins between 0.24 and 0.40, and increases in near linear fashion at closely comparable rates for the four yaw angles with  $\Psi$  until leading edge vortex initiation. At this point,  $C_{TQ}$  rise is interrupted by two influences. The first is diminishing suction in the leading edge vicinity following vortex initiation. The second is convection of the vortex and accompanying maximum suction point aftward on the blade surface. The combination of these influences reduces the magnitude of the forward directed force vector, which consequently reduces  $C_{TQ}$ . After the maximum suction point passes the S809 maximum thickness point at  $0.56c$  and the chordwise pressure distribution is approximately balanced fore and aft,  $C_{TQ}$  undergoes relatively little variation. From the point of leading edge vortex initiation,  $C_{TQ}$  decrease with  $\Psi$  is faster for higher  $\gamma$  values.

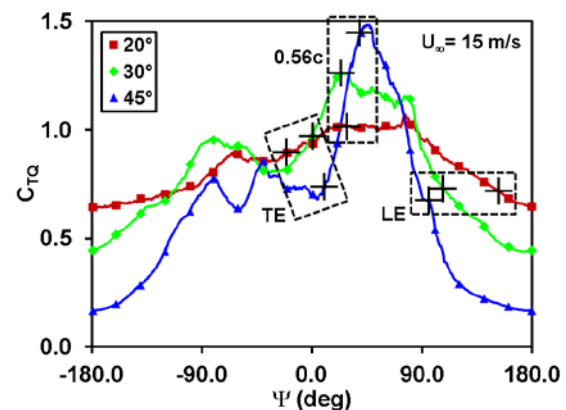
Thus, given that the rate of  $C_{TQ}$  rise and  $C_{TQ}$  decline both were faster for higher  $\gamma$  values, whereas the maximum  $C_{TQ}$  levels were comparable, the net effect was that dynamic stall enhancement of  $C_{TQ}$  appeared to peak at relatively low  $\gamma$  and then to decrease with higher values of  $\gamma$ .

Figure 14 contains three plots of  $C_{TQ}$  with  $\Psi$ , for  $U_\infty = 15$  m/s and  $\gamma = 20^\circ, 30^\circ$ , and  $45^\circ$ , all at the  $0.30R$  blade radius. Three dashed rectangles, marked “TE”, “0.56c”, and “LE” appear on the plot, each containing three large cross symbols that correspond to the three values of  $\gamma$ . The three boxes identify  $C_{TQ}$  when separation was located: 1) at the blade trailing edge, 2) at  $0.56c$  near the blade maximum thickness location, and 3) at the blade leading edge. Identification of separation location and separation chordwise movement were explained in connection with Figure 12.

In Figure 14,  $C_{TQ}$  for all three yaw angles increased in measured fashion, until approximately  $\Psi = -90^\circ$ . Here, the increase in  $C_{TQ}$  ceased and  $C_{TQ}$  remained approximately constant, until the crosses in the “TE” box were reached. At this time, the separation point began moving forward on the blade suction surface aft of the maximum thickness point. As it did so,



**Figure 13.**  $C_{TQ}$  vs. rotor azimuth plots for  $U_\infty = 10$  m/s and  $0.47R$ , at  $\gamma = 5^\circ, 10^\circ, 20^\circ$ , and  $30^\circ$ .



**Figure 14.**  $C_{TQ}$  vs. rotor azimuth plots for  $U_\infty = 15$  m/s and  $0.30R$ , at  $\gamma = 20^\circ, 30^\circ$ , and  $45^\circ$ .

suction was attenuated aft of maximum thickness and aft directed force decreased. This response increased the net forward directed force and yielded the resurgence and steep rise in  $C_{TQ}$  between “TE” and “0.56c”. As the separation point reached and passed the S809 maximum thickness point at 0.56c, suction over the forward part of the blade was reduced, which decreased the net forward directed force and prompted the rapid decline in  $C_{TQ}$  between “0.56c” and “LE”.

It is important to note that the mechanism cited to explain trends in Figure 14 is predicated on the presence of a robust surface pressure distribution over the suction surface. Without a robust surface pressure distribution over the suction surface, separation movement over the suction surface cannot substantially alter the surface pressure distribution and with it the fore-aft force balance that governs  $C_{TQ}$ . This premise is well justified, because for  $U_\infty$ ,  $\gamma$ , and  $r/R$  conditions in Figure 14, rotational augmentation enabled  $\alpha$  and  $C_n$  to reach and sustain levels that were 2 to 3 times higher than those for the static, two-dimensional stall threshold. Presence of a rotationally augmented state as well as the associated  $\alpha$  and  $C_n$  levels are consistent with the baseline trends documented in Figures 9 and 10.

#### 4. Conclusions

In the current work, EU-JOULE Project and UAE Phase VI experiment data were exploited to characterize three-dimensional, unsteady, and viscous interactions responsible for anomalous power responses to yaw error variations. Notably, key rotor and blade aerodynamic interactions were subtle, and rigorous inflow control enabled by wind tunnel experiments was essential to the success of this work. Targeted analyses of these data enabled the following observations.

In contrast to predictions based predominantly on potential flow interactions, DATA Project and UAE Phase VI data both showed nonmonotonic rotor power responses to changes in yaw. Maxima in cycle average rotor power were observed at yaw angles that deviated significantly from zero yaw.

Cycle average rotor power maxima at yawed conditions were significantly greater than levels at axisymmetric conditions. The fact that the axisymmetric conditions already were amplified by rotational augmentation testifies to the intensity of the aerodynamic interactions responsible for yawed rotor power maxima.

Anomalies in yawed rotor power were caused by dynamic stall and dynamic separation. Both of these processes were unsteady and acted only over portions of the rotor cycle. Radial locations and cycle times of occurrence varied with wind speed and yaw angle.

Though the surface pressure disturbance moved in opposite chordwise directions for dynamic stall and dynamic separation, both altered the fore-aft balance of surface pressures on the blade, and thus enhanced rotor torque production.

Higher accuracy predictions of wind turbine power performance under yawed conditions will continue to depend on having a more complete understanding of rotor and blade aerodynamics. Further experiments like those documented in the current work, along with complementary computational modeling, will provide designers with more reliable tools for predicting power production of both wind turbines and plants.

#### 5. References

- [1] Musial, W., Butterfield, C., and Jenks, M., “Effects of Leading-Edge Roughness on S809 Airfoil Rotor Performance,” SERI TP-3563, 1990.

- [2] Musial, W., Butterfield, C., and Jenks, M., "A Comparison of Two- and Three-Dimensional S809 Airfoil Properties for Rough and Smooth HAWT Rotor Operation," SERI/TP-257-3603, 1990.
- [3] Braslow, A., Hicks, R., and Harris, R., "Use of Grit-Type Boundary-Layer-Transition Trips on Wind-Tunnel Models," NASA TN D-3579, Sept. 1966.
- [4] Bak, C., Madsen, H., Fuglsang, P., and Rasmussen, F., "Double Stall," Risø-R-1043(EN), Risø National Laboratory, Roskilde, June 1998.
- [5] Schepers, J. G., "Engineering models in wind energy aerodynamics - Development, implementation and analysis using dedicated aerodynamic measurements," Ph.D. thesis, Technical University of Delft, 2012.
- [6] Dahlberg J.A. and Montgomerie B, "Research program of the Utgrunden Demonstration Offshore Wind Farm, Final report Part 2, Wake effects and other loads," Swedish Defense Research Agency, FOI, FOI 2005-02-17, 2005.
- [7] Schepers, J. G., "EU project in German Dutch Wind Tunnel," Energy Research Center of the Netherlands, ECN, ECN-RX--01-006, January 2001.
- [8] Hand, M., Simms, D., Fingersh, L., Jager, D., Cotrell, J., Schreck, S., and Larwood, S., "Unsteady Aerodynamics Experiment Phase VI: Wind Tunnel Test Configurations and Available Data Campaigns," NREL/TP-500-29955. Golden, CO: National Renewable Energy Laboratory, 2001.
- [9] Butterfield, C., Musial, W., and Simms, D., "Combined Experiment Phase I Final Report," NREL/TP-257-4655. Golden, CO: National Renewable Energy Laboratory, 1992.
- [10] Giguere, P., and Selig, M., "Design of a Tapered and Twisted Blade for the NREL Combined Experiment Rotor," NREL/SR-500-26173. Golden, CO: National Renewable Energy Laboratory, 1999.
- [11] Zell, P., "Performance and Test Section Flow Characteristics of the National Full-Scale Aerodynamics Complex 80- by 120-Foot Wind Tunnel," NASA TM 103920, January 1993.
- [12] Reuss Ramsay, R., Hoffman, M., and Gregorek, G., "Effects of Grit Roughness and Pitch Oscillations on the S809 Airfoil," NREL/TP-442-7817. Golden, CO: National Renewable Energy Laboratory, 1995.
- [13] Schreck, S., Sørensen, N., and Robinson, M., "Aerodynamic Structures and Processes in Rotationally Augmented Flow Fields," *Wind Energy*, v. 10, n. 2, March/April 2007, pp. 159-178.
- [14] Schreck, S. and Robinson, M., "Blade Three-Dimensional Dynamic Stall Response to Wind Turbine Operating Condition," *J. of Solar Energy Engineering*, v. 127, n. 4, pp. 488-495, November 2005.
- [15] Walker, J., Helin, H., and Strickland, J., "An Experimental Investigation of an Airfoil Undergoing Large Amplitude Pitching Motions," AIAA 85-0039, AIAA 23<sup>rd</sup> Aerospace Sciences Meeting, Jan. 1985.
- [16] Schreck, S., Addington, G., and Luttges, M., "Flow Field Structure and Development Near the Root of a Straight Wing Pitching at Constant Rate," AIAA 91-1793, AIAA 22<sup>nd</sup> Fluid Dynamics, Plasma Dynamics and Lasers Conference, June 1991.
- [17] Carr, L. W., "Progress in Analysis and Prediction of Dynamic Stall," *J. of Aircraft*, v. 25, n. 1, pp. 6-17. 1988.